Journal of Mining and Metallurgy, 39 (1–2) B (2003) 23 - 42.

ORDER/DISORDER IN ELECTRODEPOSITED ALUMINUM-TITANIUM ALLOYS

G. R. Stafford[*], T. Tsuda[**] and C. L. Hussey[**]

[*]*Materials Science and Engineering Laboratory, National Institute of Standards and Technology, Gaithersburg, Maryland 20899*

[**]*Department of Chemistry and Biochemistry, The University of Mississippi University, Mississippi 38677, USA*

Abstract

The composition, morphology, and crystallographic microstructure of Al-Ti alloys electrodeposited from two different chloroaluminate molten salt electrolytes were examined. Alloys containing up to 28 % atomic fraction Ti were electrodeposited at 150 °C from 2:1 $AlCl_3$-NaCl with controlled additions of Ti^{2+}. The apparent limit on alloy composition is proposed to be due to a mechanism by which Al_3Ti forms through the reductive decomposition of $[Ti(AlCl_4)_3]^-$. The composition of Al-Ti alloys electrodeposited from the $AlCl_3$-EtMeImCl melt at 80 °C is limited by the diffusion of Ti^{2+} to the electrode surface. Alloys containing up to 18.4 % atomic fraction Ti are only obtainable at high Ti^{2+} concentrations in the melt and low current densities. Alloys electrodeposited from the higher temperature melt have an ordered $L1_2$ crystal structure while alloys of similar composition but deposited at lower temperature are disordered fcc. The appearance of antiphase boundaries in the ordered alloys suggests that the deposit may be disordered initially and then orders in the solid state, subsequent to the charge transfer step and adatom incorporation into the lattice. This is very similar to the disorder-trapping observed in rapidly solidified alloys. The measured domain size is consistent with a mechanism of diffusion-controlled domain growth at the examined deposition temperatures and times.

1. Introduction

The excellent high temperature properties, low density and corrosion resistance of aluminum-based intermetallic compounds has led to the consideration of these ordered alloys for structural applications, with applications envisioned for monolithic and, more

likely, composite materials. Several processing methods have been investigated including solidification from the liquid and gas phase, mechanical alloying, reaction sintering of elemental powders and electrodeposition. Electrodeposition is an attractive method for fabricating intermetallic compounds since undesirable compositional inhomogeneities are very limited in scale and grain sizes are typically very small. Although electrodeposition is very different from traditional approaches used to fabricate these alloys, a number of analogies exist between it and rapid solidification. For example, electrodeposition from chloroaluminate electrolytes has been used to produce aluminum alloys with varying degrees of free energy relative to that of the equilibrium phases. In the Al-Mn system, amorphous [1,2], metastable crystalline [3,4], quasicrystalline [5], and stable crystalline [4,6] alloys have been electrodeposited from $AlCl_3$-NaCl electrolytes containing $MnCl_2$ at temperatures ranging from 150 to 450 °C. As the deposition temperature is increased, the excess free energy in the deposit is seen to decrease. As a consequence, equilibrium phases can be deposited at the highest deposition temperatures.

More recently it has been shown that a variety of interesting aluminum-transition metal alloys can be deposited from the Lewis acidic $AlCl_3$-1-ethyl-3-methylimidazolium chloride ($AlCl_3$-EtMeImCl) molten salt, which is liquid at ambient temperature [7-10]. Similar to the higher temperature system, several unique microstructural features such as extended solid solubility, metastable crystalline phases, and metallic glasses are observed. Based on the structural development of Al-Mn alloys deposited at high temperature, one would expect greater departures from equilibrium in deposits formed at ambient temperature. The aim of this study is to make a direct comparison of the electrodeposition process as well as the resultant crystal structure of several Al-Ti alloys electrodeposited from $AlCl_3$-NaCl at 150 °C and from $AlCl_3$-EtMeImCl at 80 °C.

2. Experimental

Al-Ti alloys were electrodeposited from both 2:1 $AlCl_3$-NaCl at 150 °C and 2:1 $AlCl_3$-EtMeImCl at 80 °C. The $AlCl_3$ (anhydrous, 99.9 %) was used after sublimation at 195 °C in the presence of helium (99.999 %, Ultra-Pure, Air Products*). The NaCl (Mallinckrodt, Analytical Reagent) was dried for 4 hours at 500 °C. All of the $AlCl_3$-EtMeImCl work was performed at the University of Mississippi and has recently been published elsewhere [11] . Some of that work is presented here to make comparisons to the high-temperature deposition process. The procedures used for the synthesis and purification of EtMeImCl have been described elsewhere [8,12]. All chemicals were stored in a Vacuum Atmospheres dry box containing ultra pure argon.

* Certain trade names are mentioned for experimental information only; in no case does it imply a recommendation or endorsement by NIST.

Al-Ti alloys were electrodeposited from $AlCl_3$-NaCl using a jacketed Pyrex cell [13,14]. Its temperature was maintained at 150 °C by a Cole Parmer Model 1268-44 Circulator, which continually pumped silicone fluid through the jacketed portion of the cell. The working and counter compartments were separated by a fine frit with an average pore size of 4 μm. The counter electrode was a 6 mm aluminum rod (99.998 %, Morton Thiokol, Inc.). The working compartment contained the following components: (1) the reference electrode assembly containing a 2.0 mm aluminum wire (99.998 %, Morton Thiokol, Inc.) immersed in 2:1 $AlCl_3$-NaCl and separated from the working electrolyte by an ultra-fine frit with an average pore size of 0.9 μm; (2) the working electrode, either a 0.75 mm titanium wire (99.98 %, Morton Thiokol, Inc.) to be electrochemically dissolved to Ti^{2+} or a 0.80 mm copper wire to serve as the substrate during electrodeposition; and (3) a magnetic stirring bar encased in Pyrex. Ti^{2+} was added to the working compartment by either the galvanostatic dissolution of the titanium wire or the direct addition of $Ti(AlCl_4)_2$, prepared by reacting Ti metal with $AlCl_3$ using the procedure of Brynestad and co-workers [15].

Al-Ti alloys were electrodeposited from 2:1 $AlCl_3$-EtMeImCl using a standard three-electrode cell. Coils of 0.10 cm diameter aluminum wire (Alfa Aesar, 99.999 %) were used for the counter and reference electrodes. These electrodes were immersed in the melt with the same composition as the bulk melt, but were separated from the bulk melt by a porosity E glass frit (Ace Glass). The aluminum electrodes were cleaned with a mixture of concentrated H_2SO_4, HNO_3, and H_3PO_4, rinsed with distilled H_2O, and dried under vacuum before use. Anhydrous titanium (II) chloride (Aldrich, 99.98 %) was used as received. All experiments were carried out in a nitrogen gas-filled glove box (VAC Atmospheres NEXUS system) with O_2 and H_2O < 5 ppm. The electrodeposition of Ti-Al alloys was performed with an EG&G PARC Model 173 potentiostat / galvanostat equipped with a Model 179 digital coulometer plug-in module.

The surface morphology of the electrodeposits was studied by scanning electron microscopy (SEM) using a JEOL JXA-840 and field-emission scanning electron microscopy (FE-SEM) using a Hitachi S-4700. Electrodeposits were also examined by x-ray diffraction (XRD) using a Siemens D-500 diffractometer and Cu-Kα radiation. The lattice parameters of the deposits were refined using the copper substrate reflections as an internal standard. Cross-sections of alloys deposited onto Cu wires were formed by first overplating with copper using a cyanide copper strike followed by bright copper from a copper sulfate electrolyte [16]. The alloy composition was determined by performing quantitative energy dispersive x-ray spectroscopy (EDS) on polished cross-sections using pure aluminum and titanium as standards. Deposits were typically 5 μm to 20 μm in thickness. Transmission electron microscopy (TEM) was performed on selected deposits prepared for both plan view and cross-sectional analysis. The plan view films were detached from a planar Cu substrate and affixed to a Mo support ring. Cross-sectional cuts, 0.75 mm thick, were cut from the overplated samples and were then

dimple polished down to 20 μm thickness. Plan view and cross-section samples were subsequently milled with 4.5 kV Ar ions at 5° incident angle. Portions of the samples with electron transparency were examined at 300 kV by TEM using a JEOL 3010.

3. Results

3.1. Deposit Composition

Figure 1 is a graph showing the composition of alloys deposited onto copper substrates as a function of Ti^{2+} concentration and current density in 2:1 $AlCl_3$-NaCl [14] and from 2:1 $AlCl_3$-EtMeImCl at a single Ti^{2+} concentration [11]. For low Ti^{2+} concentrations in $AlCl_3$-NaCl, the alloy composition is dependent upon the applied current density. An alloy having a titanium concentration of 25 % atomic fraction is deposited only at low current densities. As the current density is increased, the Ti partial current density becomes limited by the diffusion of Ti^{2+}, and the Ti content of the alloy drops. At a Ti^{2+} concentration of 150 mmol L^{-1}, the current density dependence is virtually gone, and an alloy containing 25 % atomic fraction titanium is deposited at nearly all current densities. The highest titanium concentration observed is 28 % atomic fraction. Similar behavior has been reported by Uchida and co-workers [17] in the $AlCl_3$-NaCl-KCl eutectic at 200 °C. Figure 1 also shows the alloy composition-current density relationship for deposits formed in $AlCl_3$-EtMeImCl at a Ti^{2+} concentration of 170 mmol L^{-1}. The results indicate that the diffusion-controlled deposition observed at low Ti^{2+} concentrations in $AlCl_3$-NaCl at 150 °C is extended to higher Ti^{2+} concentration in $AlCl_3$-EtMeImCl at 80 °C. This is likely due to a lower value of the Ti^{2+} diffusion coefficient in the ambient temperature melt.

Fung and Mamantov [18] attributed an observed non-linear dependence of voltammetric peak current with Ti^{2+} concentration at lower temperatures to the formation of polymeric species such as $[Ti(AlCl_4)_2]_n$. The formation of such polymers would result in a decrease of the diffusion coefficient as the concentration of Ti^{2+} is increased. They reported Ti^{2+} diffusion coefficients on the order of 2.5 x 10^{-6} cm^2 s^{-1} in $AlCl_3$-NaCl containing 170 mmol L^{-1} Ti^{2+} at 185 °C. In contrast, Tsuda has reported a value of 5.5 x 10^{-8} cm^2 s^{-1} in $AlCl_3$-EtMeImCl containing 170 mmol L^{-1} Ti^{2+} at 80 °C [11]. This lower value can be attributed to both the lower diffusion coefficients inherent to ambient temperature melts, as well as to the formation of polymeric Ti^{2+} species at the lower temperature.

There are two unusual aspects of the alloy composition data shown in Figure 1. The first is the apparent 25 % atomic fraction limit on the titanium concentration of the Ti-Al electrodeposits, an observation which has been reported by two independent groups

[14,17]. It is somewhat surprising that even at the higher Ti^{2+} concentrations in the melt, alloys having a higher titanium content are not accessible. Generally, increasing the concentration of an electroactive species results in an increased composition of that species in the alloy, particularly when that species is the minor component. The independence of alloy composition on current density is also unusual and is generally the result of compound formation or an indication that the two deposition reactions have similar kinetics (equal Tafel slopes).

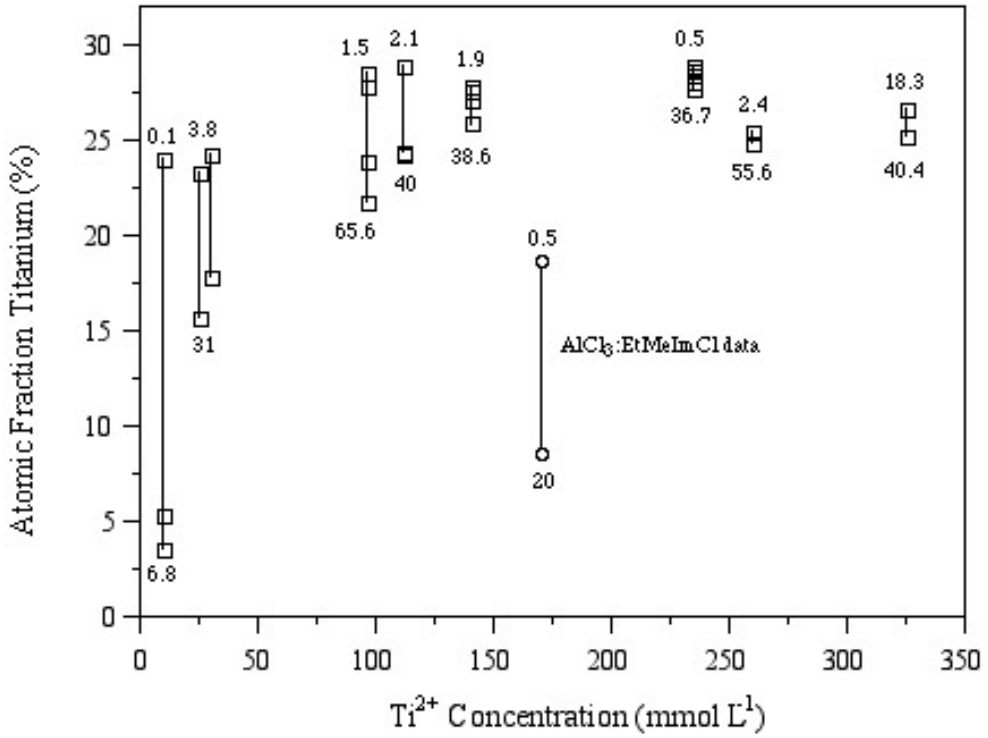

Figure 1. Alloy composition as a function of Ti^{2+} concentration in 2:1$AlCl_3$-NaCl at 150 °C (□), and from 2:1 $AlCl_3$-EtMeImCl at 80 °C and a single Ti^{2+} concentration (○). The range of deposition current densities used at each Ti^{2+} concentration is also listed in mA cm^{-2}.

Both the alloy composition and its independence on the current density can be explained if we introduce the concept of a single electroactive species having the structure and stoichiometry proposed by Seddon et al. [19,20], in this case $[Ti(AlCl_4)_3]^-$. This implies that Al_3Ti forms by the reductive decomposition of $[Ti(AlCl_4)_3]^-$. There are obvious problems with this mechanism. In acidic chloroaluminate melts, the electroactive aluminum species is $Al_2Cl_7^-$ while the more stable $AlCl_4^-$ is

reduced at potentials about 0.5 V more negative [21]. Since these alloys are electrodeposited at potentials just negative of the $Al_2Cl_7^-$ reversible potential, the reductive decomposition of $[Ti(AlCl_4)_3]^-$ would have to occur at potentials that are several hundred millivolts positive of the $AlCl_4^-$ reversible potential. In addition, this deposition mechanism is in stark contrast to that observed for Al-Mn and Al-Cr where a variety of structures and alloy compositions well beyond Al_3Mn and Al_3Cr are accessible. Although it is likely that Mn^{2+}, Cr^{2+}, and Ti^{2+} form similar solvated structures in acidic melts, the exact nature of their interactions with the available $AlCl_4^-$ and $Al_2Cl_7^-$ ligands may vary significantly.

3.2. Deposit Morphology

The morphologies of several alloys, deposited from both electrolytes under a variety of deposition conditions are shown in Figure 2. Figure 2(a) – (c) show alloys deposited from $AlCl_3$-NaCl whereas Figure 2(d) – (f) show alloys deposited from $AlCl_3$-EtMeImCl. In all cases, the deposits are dense and nodular, showing little, if any, porosity. EDS measurements detected no chlorine in the deposits, an indication that the deposits have no entrained salts. The nodule size is influenced by both the deposition current density and the titanium content of the deposit. For example, significant grain refinement can be induced by galvanostatic pulsing, Figure 2(a) and (b). Figure 2(d) and (e) show the morphology change when the current density was decreased from 20 mA cm^{-2} to 0.5 mA cm^{-2}. This corresponded to a Ti increase from 7 % to 18.4 % atomic fraction. The nodules show crystallographic faceting, although no symmetry characteristic of a particular growth direction was observed. It is clear that the nodule size decreases with decreasing current density and increasing titanium content. Typically one would expect an increase in grain size as the deposition current density or overpotential is decreased. However, in this case the grain refinement is driven by the incorporation of Ti into the alloy rather than the deposition overpotential. This nicely demonstrates the impact that impurities and alloying additions have on deposit morphology.

Interesting structural features can be seen in alloys electrodeposited at very small current densities. Since small current densities generally lead to poorly nucleated deposits, a higher current density pulse is typically required to properly nucleate the surface. Figure 2(c) shows crystallographic growth of an Al_3Ti nodule in $AlCl_3$-NaCl. A high magnification view of the 18.4 % atomic fraction Ti deposit grown in $AlCl_3$-EtMeImCl (Figure 2(e)) is shown in Figure 2(f). The step faceting is clearly seen in each nodule, confirming that the nodules are single crystals. It also suggests that although the macro-deposit grows by three-dimensional nucleation and growth, each nodule grows primarily by two-dimensional, layered growth.

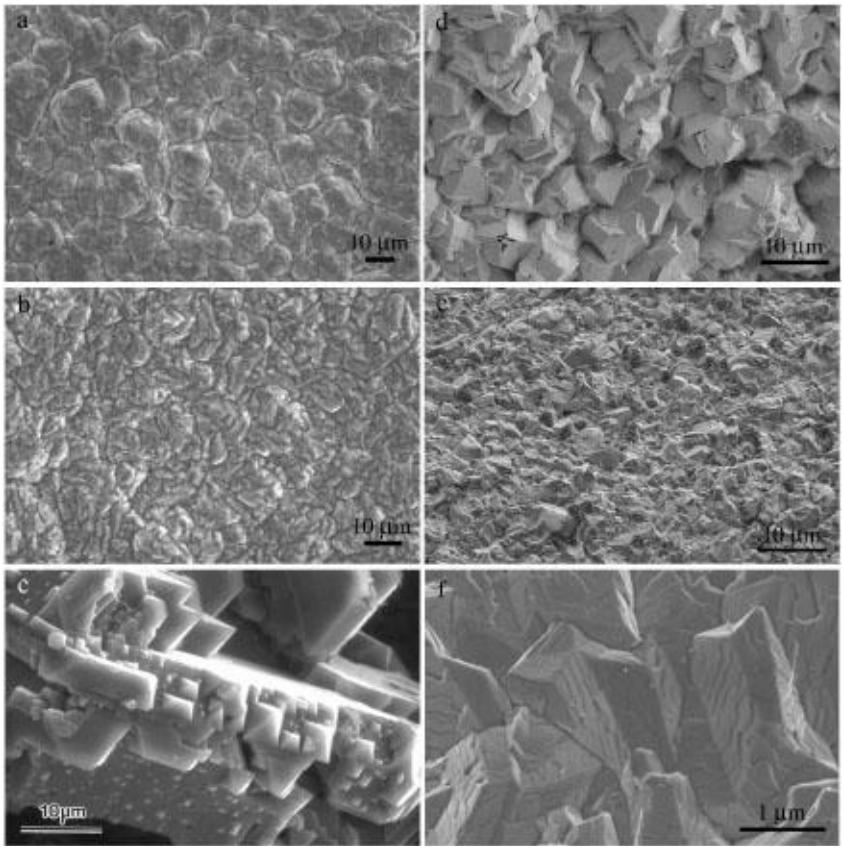

Figure 2. Scanning electron micrographs of Al-Ti alloys electrodeposited from (a-c) 2:1 $AlCl_3$-NaCl electrolyte at 150 °C and (d-f) 2:1 $AlCl_3$-EtMeImCl electrolyte at 80 °C; (a) 26.7 % Ti, 15.4 mA cm^{-2}, 220 mmol L^{-1} Ti^{2+}; (b) 26.1 % Ti, pulsed between 0 and 26.6 mA cm^{-2} for 0.1 msec at each current density, 140 mmol L^{-1} Ti^{2+}; (c) 27.8 % Ti, 0.2 mA cm^{-2}, 278 mmol L^{-1} Ti^{2+}; (d) 7.0 % Ti, 20.0 mA cm^{-2}, 170 mmol L^{-1} Ti^{2+}; (e) 18.4 % Ti, 0.5 mA cm^{-2}, 170 mmol L^{-1} Ti^{2+}; (f) 18.4 % Ti, 0.5 mA cm^{-2}, 170 mmol L^{-1} Ti^{2+}.

3.3. Deposit Crystal Structure

The crystal structure of several Al-Ti electrodeposits was determined by both x-ray and electron diffraction. X-ray patterns from deposits produced from both melts are shown in Figure 3. The current density and deposition time for each deposit are listed

with each diffraction pattern. There was no evidence of the equilibrium $D0_{22}$ Al_3Ti phase (body centered tetragonal, a_o = 0.384 nm and c_o = 0.858 nm) in any of the diffraction patterns or the high temperature variant $Al_{24}Ti_8$ identified by van Loo and Rieck [22] (tetragonal, a_o = 0.388 nm and c_o = 3.384 nm). All of the patterns show the fundamental face-centered cubic (fcc) reflections in positions very close to that of pure aluminum. The lattice parameters calculated from these reflections vary from 0.405 nm for pure aluminum to 0.400 nm for the deposits containing 25 % atomic fraction Ti. The shrinkage of the lattice with increasing Ti addition is expected as the smaller Ti atoms substitute for Al in the fcc lattice. The relative position of the 111 fundamental reflections in Figure 3 reflects the Ti content of the electrodeposit. The alloys electrodeposited from the higher temperature $AlCl_3$-NaCl melt, Figure 3(b-e) also show the 100 and 110 reflections indicative of $L1_2$ ordering. The presence of these superlattice reflections indicates that the crystal structure is not disordered fcc because the 100 and 110 reflections are forbidden in fcc. The $L1_2$ structure, stoichiometrically Al_3Ti, is comprised of titanium atoms at the corners and aluminum atoms at the face-centers of an fcc unit cell. Superlattice reflections are not present in any of the alloys electrodeposited from the lower temperature $AlCl_3$–EtMeImCl melt, Figure 3(a). For comparison, a calculated diffraction pattern [23] for fully ordered ($L1_2$) Al_3Ti is shown, Figure 3(f).

The superlattice reflections shown in Figure 3(b-e) are typically very broad, the extent of the broadening appears to be influenced by the deposition conditions. Extensive broadening of the superlattice reflections might make them difficult to detect by x-ray diffraction. A report in the literature describing a glancing angle x-ray examination of Ti-Al alloys electrodeposited from eutectic $AlCl_3$-NaCl-KCl containing Ti^{3+} also shows the fundamental reflections for fcc Al for compositions up to 27.5 % atomic fraction Ti. However, the authors were unable to confirm the $L1_2$ structure due to the lack of superlattice reflections in the x-ray diffraction pattern [17]. Whereas broadening of fundamental reflections generally indicates limited crystallite size, the broadening of superlattice reflections suggests that the $L1_2$-ordered domains are very small. One might expect that a low deposition current density might lead to more extensive ordering since surface rearrangement could occur under the reduced flux of metal atoms. This appears to be contradicted by alloys (c) and (e) which were deposited at similar current densities. Deposit (e) shows relatively well-defined superlattice reflections, while those in (c) show significant broadening. The primary difference between these two samples is the thickness of the deposit, and as a result, the time that the deposit is exposed to the elevated temperature of the molten salt. Although there does not appear to be a systematic correlation between the deposition time and superlattice reflection shape, it is clear that the domains are better defined in the deposit that was exposed for the longest time at 150 °C.

Electron diffraction was used to further characterize the ordering in the $AlCl_3$-NaCl deposits as a function of Ti content. Examples of [001] zone axis diffraction patterns are

shown in Figure 4, along with a labeled schematic [13]. All of the deposits have intense 200 and 220 (and higher order) spots, which form a square grid. The 100 reflections are not visible for the 3 % atomic fraction Ti alloy, but are observed in the other binary alloys. These superlattice reflections grow progressively more intense relative to the 200 spots as the titanium concentration is increased.

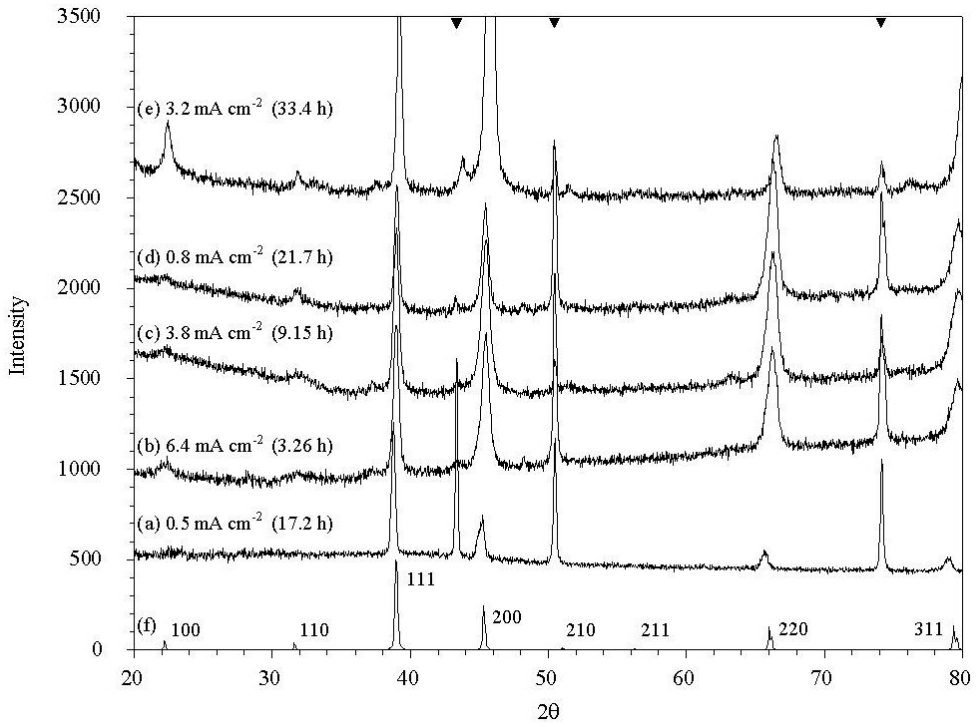

Figure 3. X-ray diffraction patterns (Cu Kα) of Al-Ti alloys electrodeposited from (a) 2:1 $AlCl_3$-EtMeImCl electrolyte containing 170 mmol L^{-1} Ti^{2+} at 80 °C and (b-e) 2:1 $AlCl_3$-NaCl electrolyte containing 150 mmol L^{-1} Ti^{2+} at 150 °C. The composition, current density and total charge for the deposits are (a) 18.4 % Ti, 0.5 mA cm^{-2}, 31.0 C cm^{-2}; (b) 25.1 % Ti, 6.4 mA cm^{-2}, 75.3 C cm^{-2}; (c) 25.8 % Ti, 3.8 mA cm^{-2}, 125.3 C cm^{-2}; (d) 26.3 % Ti, 0.8 mA cm^{-2}, 62.5 C cm^{-2}; (e) 23.5 % Ti, 3.2 mA cm^{-2}, 385.0 C cm^{-2}; (f) calculated diffraction pattern for fully ordered ($L1_2$) Al_3Ti [23]. Copper reflections from substrate denoted by (▼) at the top of the figure [51].

The electron diffraction intensity data can be interpreted by considering the structure factors of the fcc and $L1_2$ crystal structures [13]. The structure factors for Al_3Ti with the $L1_2$ and fcc crystal structures are:

$$I \alpha F^2 = (3f_{Al} + f_{Ti})^2 \text{ for fundamental reflections (fcc and } L1_2) \quad [1]$$

$$I \alpha F^2 = (f_{Al} - f_{Ti})^2 \text{ for superlattice reflections } (L1_2) \quad [2]$$

$$I \alpha F^2 = 0 \text{ for superlattice reflections (fcc)} \quad [3]$$

where I is the intensity of a given reflection, F is the structure factor, f_{Al} is the scattering factor for the Al lattice sites, and f_{Ti} is the scattering factor for the Ti lattice sites.

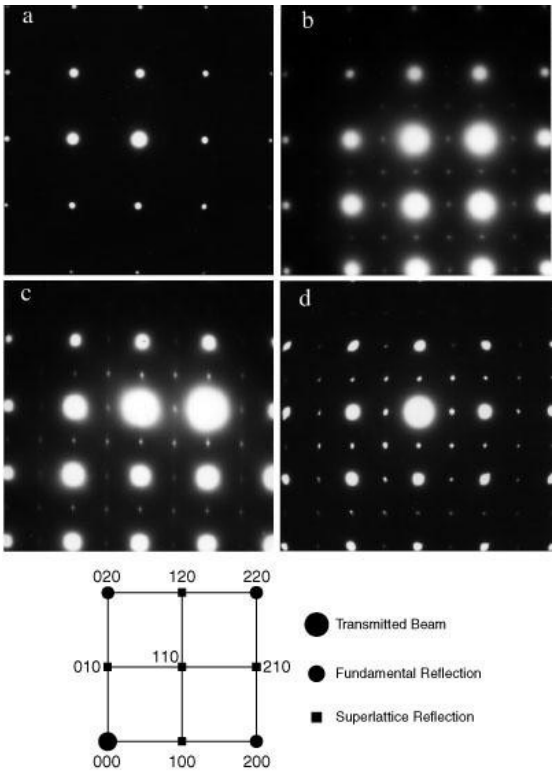

Figure 4. Selected area diffraction patterns of Ti-Al alloys electrodeposited from 2:1 $AlCl_3$-NaCl electrolyte at 150 °C. The patterns were taken on the [001] zone axis and show the increasing relative intensity of the superlattice reflections with increasing Ti content; (a) 3 % Ti, (b) 5 % Ti, (c) 16 % Ti, and (d) 24 % Ti. A labeled schematic of the diffraction pattern is shown [13].

The scattering factor for a lattice site is the weighted average of the atomic scattering factors of the atoms that occupy it. Since some of the titanium lattice sites must be occupied by aluminum atoms in the substoichiometric alloys (assuming all lattice sites are occupied), the difference in the scattering factors for the two sites and, therefore, the superlattice reflection intensities must decrease. This is in qualitative agreement with the

experimental observations. It is not possible to ascertain if the apparent absence of superlattice reflections in the 3.6 % atomic fraction Ti specimen is due to low intensity or to a disordered crystal structure because of the loss of superlattice reflection intensity at low Ti concentrations.

To confirm the chemical disorder in the Al-Ti alloys deposited from $AlCl_3$–EtMeImCl melt, electron diffraction analysis of selected electrodeposits in both plan view and cross-section was performed [11]. A typical diffraction pattern taken on the [001] zone axis from a deposit containing 18.4 % atomic fraction Ti is shown in Figure 5(a). The pattern is consistent with single phase fcc Al-Ti. No superlattice reflections were found in any of the diffraction patterns indicating that the detected phase has a random ordering of Al and Ti atoms. For comparison, the diffraction patterns from films containing 16 % and 24.0 % atomic fraction Ti, both deposited from $AlCl_3$-NaCl at 150 °C are shown in Figures 5(b) and 5(c), respectively [13]. It is also clear from Figure 5 that the chemical disorder of the room temperature melt deposit is not simply due to the sub-stoichiometric Ti content. The 16 % atomic fraction Ti alloy deposited from $AlCl_3$-NaCl clearly shows the superlattice reflections indicative of $L1_2$ ordering, Figure 5(b), even though the composition is less than that of stoichiometric Al_3Ti.

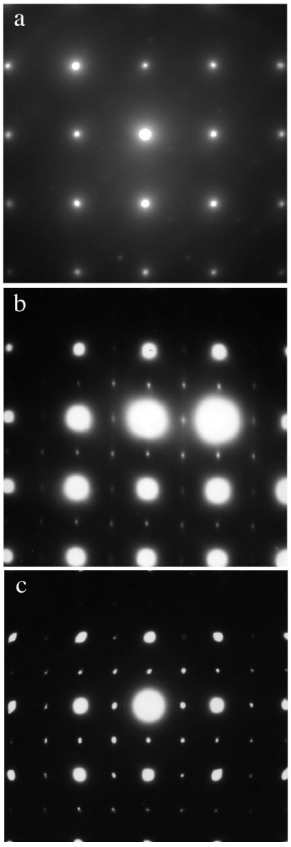

Figure 5. Selected area diffraction patterns of Ti-Al alloys taken on the [001] zone axis from as-deposited Ti-Al alloys containing: (a) 18.4 % Ti and deposited from $AlCl_3$ - EtMeImCl at 80 °C, (b) 16 % Ti and deposited from $AlCl_3$-NaCl at 150 °C, and (c) 24.0 % Ti and deposited from $AlCl_3$ - NaCl at 150 °C [13].

The microstructure of fully stoichiometric alloys electrodeposited from $AlCl_3$-NaCl consists of fine grains ranging from 0.1 μm to 0.5 μm in size. Careful examination of selected area diffraction patterns in Figure 4 reveals that both fundamental and superlattice reflections are diffuse, and in many cases the superlattice reflections have elongated shape. These features of reciprocal space suggest the presence of heterogeneities in the deposit microstructure. High-resolution imaging of the structure based on both fundamental and superlattice reflections, Figure 6(a), reveals a perfectly square lattice [24]. This suggests that the heterogeneities come from ordering imperfections. The $L1_2$ ordering appears as variations in the intensities of the bright dots (the bright dots correspond to rows of atoms projected along the direction of an electron beam, as supported by high-resolution image simulations). In order to enhance imaging of the ordering, the experimental image recorded with a charge-coupled device (CCD) camera (Figure 6(a)) was processed using Fourier transforms. First, the direct Fourier transform was obtained, and then the image was reconstructed by inverse-Fourier transform using only the <100> superlattice reflection. The inverse-Fourier transformed image, Figure 6(b), clearly reveals regions that are translated to each other by half the periodicity of the unit cell. These regions are believed to be the antiphase domains of the $L1_2$ order regions. The size of the domains is about 5 nm to 10 nm, which corresponds closely to the size of the heterogeneities observed by dark-field imaging. Consequently, the diffuseness of reflections can be understood as resulting from the spatially limited extent of long-range order.

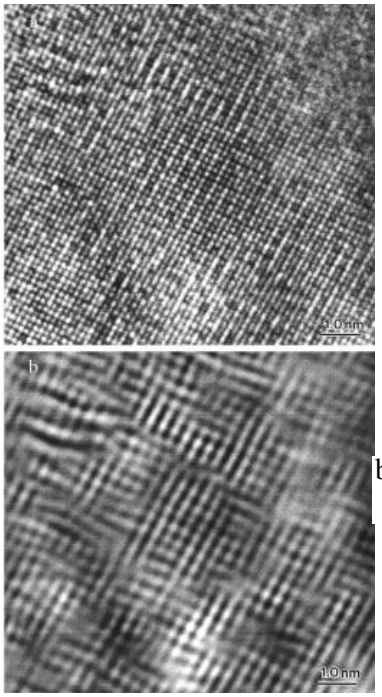

a)

b)

Figure 6. (a) High-resolution image of as-deposited Al_3Ti alloy (from 2:1 $AlCl_3$ - NaCl) on the [001] zone axis, digitally recorded with a CCD camera. (b) Filtered inverse Fourier transform of image shown in (a). The image was formed with the direct spot and super lattice 010 and 100 reflections [24].

4. Discussion

The Al-Ti phase diagram [25] indicates that the solubility of Ti in fcc Al is about 0.7 % atomic fraction at 660 °C and decreases rapidly at lower temperatures. The line compound Al_3Ti (DO_{22}) is the next phase in order of increasing Ti content. Thus, the equilibrium structure of electrodeposits containing less than 25 % atomic fraction Ti is two-phase fcc Al (saturated with Ti) and DO_{22} Al_3Ti. Likewise the 25 % atomic fraction Ti deposit should be single-phase DO_{22} Al_3Ti. Consequently, the structures observed in this study are non-equilibrium in two senses: they are single phase and the crystalline phase is either disordered fcc or ordered $L1_2$ rather than DO_{22}. The deposition of an ordered $L1_2$ phase is not surprising because small amounts of transition elements have been found to change the equilibrium structure of Al_3Ti-based alloys from DO_{22} to $L1_2$, which suggests that there is a very small difference in free energy between the two phases [26-28]. Fu [29] showed that the energy difference between binary Al_3Ti in the two crystal structures $L1_2$ and DO_{22} is quite small, about 2.4 kJ mol^{-1}. Asta has reported similar energy differences in his *ab initio* study of phase stability in the Al-Ti system [30]. The magnitude of the energy difference between Al_3Ti in the $L1_2$ and DO_{22} structures suggests that it should be possible to form $L1_2$ Al_3Ti in a binary alloy using non-equilibrium processing. The chemically disordered fcc structure obtained from the ambient temperature melt is a significant departure from the ordered $L1_2$ crystal structure deposited from $AlCl_3$-NaCl at 150 °C and suggests that larger departures from equilibrium can be obtained at lower deposition temperatures. Asta has calculated the energy difference between disordered Al_3Ti and the equilibrium DO_{22} structure to be 16.9 kJ mol^{-1} (i.e., 14.6 kJ mol^{-1} between disordered Al_3Ti and the $L1_2$ structure).

Metastable or unstable structures are formed by raising the free energy of the starting materials and then removing that energy rapidly enough to ensure that the atomic mobility is sufficiently low to prevent or limit subsequent transformations [31]. The many fabrication processes which allow one to maintain these structures can generally be divided into three categories: quenching, molecular deposition, and external action (deformation, irradiation, or chemical attack) [32]. In rapid solidification the cooling rate is primarily a function of the smallest dimension of the sample and the medium used to remove the heat. Unless an amorphous phase is retained, nucleation seems to limit the degree of super-cooling to about 30 % of the melting temperature; i.e., $\Delta T/T_m = 0.3$ [33]. Based on this limitation, it is generally impossible to produce a metastable crystalline phase from the melt having an excess free energy relative to the equilibrium form larger than ~ 0.3 ΔH_m (~3.0 kJ mol^{-1}), where ΔH_m is the enthalpy of melting [34,35]. The fact that the $L1_2$ phase has not been observed in rapidly solidified binary alloys [36,37] is most probably due to the fact that the energy difference between the $L1_2$

and DO_{22} crystal structures (2.4 kJ mol^{-1}) approaches the excess free energy limit of this technique (3.0 kJ mol^{-1}).

Based on the formation energies discussed above, one would not expect Al_3Ti to form a disordered fcc structure by rapid solidification. Boettinger has developed the theory that describes the trapping of disorder in intermetallic phases by rapid solidification [38]. Equation [4] describes the critical solidification velocity, V, which results in the crystallization of a disordered alloy, where T_c is the critical order-disorder transformation temperature, T_m is the melting point of the solid, and V_d is a kinetic rate parameter for crystallization. V_d is typically taken as the speed of liquid interdiffusion (D_L/λ) where D_L is the liquid diffusion coefficient and λ is the jump distance. The T_c/T_m for $L1_2$ Al_3Ti is estimated to be about 1.8 . Assuming a V_d value of 200 cm s^{-1} (D_L = 6 x 10^{-6} cm^2 s^{-1}, λ = 3 x 10^{-8} cm), one calculates a critical solidification velocity of 160 cm s^{-1}. Such a velocity is typically difficult to achieve in rapid solidification from the melt.

$$\frac{V}{V_d} = \frac{T_c}{T_m} - 1 \qquad [4]$$

In condensation, vapor deposition, or sputtering, the extent of supercooling possible is much greater that that from the melt. In addition, the enthalpy of vaporization is generally an order of magnitude larger than that of melting. Consequently, one can produce metastable crystalline phases having an excess free energy on the order of ~50.0 kJ mol^{-1}, making vapor condensation a potentially much more powerful method for crystalline phase retention than melt solidification [34,35]. While exact correlations between electrodeposition and vapor deposition have not been developed, the excess free energy possible in alloys produced by these two techniques is similar [34,39]. Electrodeposited alloys are rarely in equilibrium and one can assume that at least a portion of the activation overpotential is used to increase the free energy of the deposit relative to that of the equilibrium phase. The extra energy required to electrodeposit Al_3Ti in the $L1_2$ (2.4 kJ mol^{-1}) and disordered fcc (16.9 kJ mol^{-1}) structures rather than the equilibrium DO_{22} structure would require a minimum overpotential of 9 mV and 64 mV respectively. These are clearly accessible deposition overpotentials and add some justification for the metastable structures observed in these electrodeposits.

Although it is clear that the excess free energy observed in these Al-Ti alloys can be achieved through electrodeposition, the actual mechanism by which these structures are electrochemically formed remains unclear, particularly since these deposits display crystallographic features of distinctly different length scales. The grain size of all electrodeposits examined in this study is on the order of 0.5 μm to 5 μm. Deposits formed at 80 °C are chemically disordered while those formed at 150 °C have $L1_2$ domains measuring 5 nm to 10 nm in size. The image in Figure 6(b) suggests that these domains appear to

have grown through a first order nucleation and growth process, independent of the electrocrystallization process. This type of domain structure is quite common in rapidly solidified alloys wherein the disordered phase produced by the solidification process transforms to the equilibrium ordered phase quite rapidly during solid-state cooling to room temperature [40]. Although this often occurs at temperatures that do not allow for significant bulk diffusion, the activation barrier to the nucleation of ordered domains is rather small because both the nucleus and matrix have essentially the same crystal structure and composition [41]. Consequently, nucleation tends to be homogeneous and independent of lattice defects.

Cu_3Au is the classic system for studying first-order compositional order-disorder transformations. Similar to electrodeposited Al_3Ti, Cu_3Au forms an $L1_2$ structure in the ordered state. When quenched from above the critical (order-disorder transformation) temperature to room temperature, Cu_3Au retains the disordered structure. Annealing the disordered alloy below the critical temperature, causes ordering to occur through the nucleation and growth of ordered regions at different points throughout the crystal. These small ordered regions grow by consuming the disordered material until they impinge to form a domain structure, similar to that shown in Figure 6(b). There is considerable experimental evidence in the literature suggesting that antiphase domain growth is analogous to classical metallurgical grain growth [42-45] in that it follows the relation,

$$D^2 - D_o^2 = 2Kt \qquad [5]$$

where D is the domain size (diameter), and D_o is the domain size at $t = 0$. The rate constant K has an Arrhenius-type temperature dependence and is proportional to the free energy of the domain boundary and its mobility. In a given domain, the boundary advances when the atoms in anti-phase positions in the domain being consumed jump the required distance and become in-phase with the other atoms in the growing domain. In a binary ordered alloy, both atomic species will be required to jump for the boundary to advance. Consequently, the process of antiphase domain growth is typically viewed to be diffusion-controlled. The activation energy for domain growth in Cu_3Au has been measured at 184 kJ mol^{-1} which is consistent with bulk diffusion in the alloy [42,43]. Cahn has made a direct comparison of the interdiffusion coefficient and the time derivative of the square of the domain size in Cu_3Au and determined that they are essentially identical in the temperature range of 300 °C to 375 °C [46].

Assuming that the Ti-Al alloys deposit in the disordered state and that ordering occurs in the solid state, the degree of chemical order-disorder would be directly linked to the deposition temperature and the time at which the deposit remains at the elevated temperature during deposition. At first glance it would seem that there is little difference between 80 °C and 150 °C with regards to diffusional processes, both temperatures are

rather low. If we assume that K in equation [5] is thermally activated (i.e., $K = K_o \exp(-Q/RT)$), then the activation energy (Q) required to produce a 5 nm domain size at 150 °C and a disordered deposit (< 0.1 nm domain size) at 80 °C is 138 kJ mol^{-1}. This is consistent with a thermally activated diffusion process.

This analysis can be taken a step further with knowledge of the Al and Ti diffusivity in fcc Al_3Ti. Unfortunately, this data does not exist and diffusion coefficients from chemically related systems are only available for temperatures exceeding 350 °C. Extrapolation of high-temperature data to temperatures less than 150 °C may not be valid since alternative mechanisms such as grain boundary, dislocation, and surface diffusion may become dominant at lower temperatures. However, since the domains shown in Figure 6(b) are much smaller than the grain size, it is likely that a vacancy-exchange mechanism is operative during the ordering process and that high-temperature data can be used to quantify domain growth.

Figure 7 is an Arrhenius plot comparing the domain size observed in electrodeposited Al_3Ti to literature values of the diffusion coefficients of similar chemistries. The

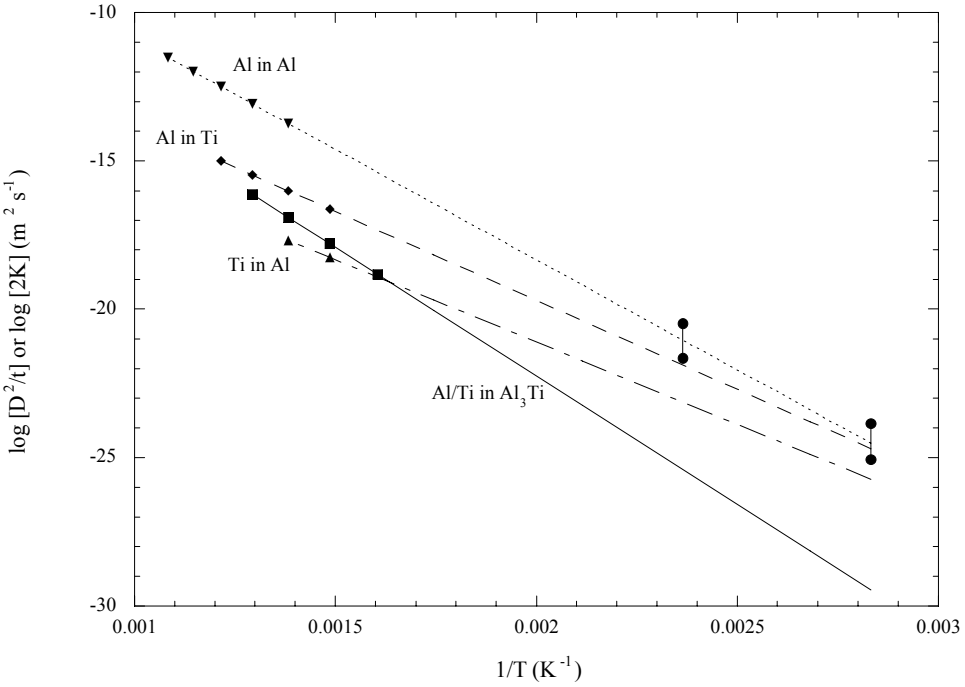

Figure 7. Arrhenius plots of (●) log (D^2/t) from this study where D is the observed domain size and t is a typical range of deposition times (2 to 30 h); and log (2K) where K is a literature value of the diffusion coefficient of (▲) Ti in Al [47], (◆) Al in Ti [48], (▼) Al in Al [49], and (■) interdiffusion coefficient of Ti and Al in Al_3Ti [50]. The lines are an extrapolation of the literature data to the deposition temperature range examined in this study.

experimental data is plotted as log (D^2/t) where D is the domain size and t is a typical range of deposition times (2 to 30 h). The domain size is assumed to be 5 nm at 150 °C (this will obviously be a function of deposition time) and less than 0.1 nm at 80 °C (disordered). Data from several diffusion couples are also plotted as log (2K) where K is the literature value of the intrinsic diffusion coefficient of Ti in Al [47], Al in Ti [48], Al in Al [49], and the interdiffusion coefficient of Ti and Al in Al_3Ti [50]. The lines are an extrapolation of the literature data to the deposition temperature range examined in this study. The kinetics for Al self-diffusion as well as the diffusion of Al in pure Ti is sufficiently fast to account for the ordering phenomena observed in the electrodeposited alloys whereas the kinetics for Ti diffusion in pure Al as well as the interdiffusion of Ti and Al in Al_3Ti would not appear to support ordering at these relatively low temperatures. Although one might expect the Al_3Ti diffusion data to best describe our experimental system, the former data is based on an alloy that has the ordered DO_{22} structure. The chemical ordering as well as the smaller lattice volume inherent to this structure may alter the diffusion kinetics; consequently diffusion in disordered Al_3Ti may be expected to behave differently.

5. Summary

The composition, morphology and crystallographic structure of Al-Ti alloys electrodeposited from two different chloroaluminate molten salt electrolytes were examined. Alloys containing up to 28 % atomic fraction Ti were electrodeposited at 150 °C from 2:1 $AlCl_3$-NaCl with controlled additions of Ti^{2+}. The apparent limit on alloy composition is proposed to be due to a mechanism by which Al_3Ti forms through the reductive decomposition of $[Ti(AlCl_4)_3]^-$. The composition of Al-Ti alloys electrodeposited from the $AlCl_3$-EtMeImCl melt at 80 °C is limited by the diffusion of Ti^{2+} to the electrode surface. Alloys containing up to 18.4 % atomic fraction Ti are only obtainable at high Ti^{2+} concentrations in the melt and low current densities. Al-Ti electrodeposited from the higher temperature melt has an ordered $L1_2$ crystal structure while alloys of similar composition but deposited at lower temperature are disordered fcc. The appearance of antiphase boundaries in the ordered alloys suggests that the deposit may be disordered initially and then orders in the solid state, subsequent to the charge transfer step and adatom incorporation into the lattice. This is very similar to the disorder-trapping observed in rapidly solidified alloys. The measured domain size is consistent with a mechanism of diffusion-controlled domain growth at the examined deposition temperatures and times.

6. Acknowledgements

The authors gratefully acknowledge the technical contributions of Leo Bendersky, John Bonevich, Bill Boettinger, Ursula Kattner, and Carelyn Campbell at NIST and Gregg Janowski at the University of Alabama at Birmingham. CLH and TT acknowledge the financial support of the Air Force Office of Scientific Research.

References

1. Stafford, G.R., J. Electrochem. Soc., 136(3): p. 635 (1989).
2. Grushko, B. and Stafford, G.R., Metall. Trans. A, 20A(8): p. 1351 (1989).
3. Grushko, B. and Stafford, G.R., Scr. Metall., 23(4): p. 557 (1989).
4. Stafford, G.R., Grushko, B., and McMichael, R.D., J. Alloys Compd., 200(1-2): p. 107 (1993).
5. Grushko, B. and Stafford, G.R., Scr. Metall., 23(7): p. 1043 (1989).
6. Grushko, B. and Stafford, G.R., Metall. Trans. A, 21A(11): p. 2869 (1990).
7. Pitner, W.R., Hussey, C.L., and Stafford, G.R., J. Electrochem. Soc., 143(1): p. 130 (1996).
8. Tierney, B.J., Pitner, W.R., Mitchell, J.A., Hussey, C.L., and Stafford, G.R., J. Electrochem. Soc., 145(9): p. 3110 (1998).
9. Zhu, Q., Hussey, C.L., and Stafford, G.R., J. Electrochem. Soc., 148: p. C88 (2001).
10. Mitchell, J.A., Pitner, W.R., Hussey, C.L., and Stafford, G.R., J. Electrochem. Soc., 143(11): p. 3448 (1996).
11. Tsuda, T., Hussey, C.L., Stafford, G.R., and Bonevich, J.E., J. Electrochem. Soc., 150: p. C234 (2003).
12. Xu, X.H. and Hussey, C.L., J. Electrochem. Soc., 140(3): p. 618 (1993).
13. Janowski, G.M. and Stafford, G.R., Metall. Trans. A, 23A(10): p. 2715 (1992).
14. Stafford, G.R., J. Electrochem. Soc., 141(4): p. 245 (1994).
15. Brynestad, J., von Winbush, S., Yakel, H.L., and Smith, G.P., Inorg. Nucl. Chem. Lett., 6: p. 889 (1970).
16. Durney, L.J. 4th ed. Electroplating Engineering Handbook. 1984: Van Nostrand Reinhold Co., New York. 185.
17. Uchida, J., Seto, H., and Shibuya, A., J. Surf, Fin. Soc. Japan, 46: p. 1167 (1995).
18. Fung, K.W. and Mamantov, G., J. Electroanal. Chem., 35: p. 27 (1972).
19. Dent, A.J., Seddon, K.R., and Welton, T., J. Chem. Soc., Chem. Commun.: p. 315 (1990).
20. Abdul-Sada, A., Greenway, A., Seddon, K., and Welton, T., Org. Mass Spectrom., 27: p. 648 (1992).
21. Stafford, G.R. and Haarberg, G.M., Plasmas and Ions, 1: p. 35 (1999).

22. van Loo, F.J.J. and Rieck, G.D., Acta Metall., 21: p. 61 (1973).
23. Smith, D.K., Nichols, M.C., and Zolensky, M.E., A Fortran IV Program for Calculating X-ray Powder Diffraction Patterns - Version 10, Department of Geosciences, The Pennsylvania State University, University Park, Pennsylvania, March, 1983.
24. Stafford, G.R., Bendersky, L.A., and Janowski, G.M., in Defect Structure, Morphology, and Properties of Vapor and Electrodeposits, H.D. Merchant, p. 231, The Minerals, Metals and Materials Society, (1994).
25. Massalski, T.B., ed. Binary Alloy Phase Diagrams. 1986, American Society of Metals: Metals Park, OH.
26. Raman, A. and Schubert, K., Z. Metallkd., 56: p. 99 (1965).
27. Kumar, K.S. and Pickens, J.R., Ternary Low-density Cubic L12 Aluminides, in Dispersion Strengthened Aluminum Alloys, Y.-W. Kim and W.M. Griffith, Editors. 1988, The Minerals, Metals & Materials Society.
28. Powers, W.O. and Wert, J.A., Met. Trans., 21A: p. 145 (1990).
29. Fu, C.L., J. Mater. Res., 5: p. 971 (1990).
30. Asta, M., de Fontaine, D., and Schilfgaarde, v., J. Mater. Res., 8: p. 2554 (1993).
31. Spaepen, F., Science, 235: p. 1010 (1987).
32. Jones, H., in Second International Conference on Rapidly Quenched Metals, B.C. Giessen and N.J. Grant, 1, MIT Press, Cambridge, MA, (1976).
33. Hollomon, J.H. and Turnbull, D., Prog. Metal. Phys., 4: p. 333 (1953).
34. Baker, J.C. and Cahn, J.W., Thermodynamics of Solidification. 1971, Metals Park, OH: American Society of Metals.
35. Sinha, A.K., Giessen, B.C., and Polk, D.E., Metastable Phases Prodiced by Rapid Quenching from the Vapor and the Liquid. Treatise on Solid State Chemistry, ed. N.B. Hannay. Vol. 3. 1976.
36. Hanamura, T., Sugai, T., and Tanino, M., J. of Materials Science, 25: p. 3286 (1990).
37. Hall, E.L. and Huang, S.-C., Acta metall. mater., 38: p. 539 (1990).
38. Boettinger, W.J. and Aziz, M.J., Acta metall., 37(12): p. 3379 (1989).
39. Polk, D.E. and Giessen, B.C., Metallic Glasses. 1978, Metals Park, OH: American Society of Metals.
40. Boettinger, W.J., Bendersky, L.A., Cline, J., West, J.A., and Aziz, M.J., Mater. Sci. Eng., A, 133: p. 592 (1991).
41. Porter, D.A. and Easterling, K.E., Phase Transformations in Metals and Alloys. 1981, Berkshire, UK: Van Nostrand Reinhold Co., Ltd.
42. Poquette, G.E. and Mikkola, D.E., Trans. Met. Soc. AIME, 245: p. 743 (1969).
43. Sakai, M. and Mikkola, D.E., Met. Trans., 2: p. 1635 (1971).
44. Nagler, S.E., Shannon, J., R. F., Harkless, C.R., Singh, M.A., and Nicklow, R.M., Phys. Rev. Lett., 61: p. 718 (1988).
45. Ardell, A.J., Mardesich, N., and Wagner, C.N.J., Acta metall., 27: p. 1261 (1979).

46. Cahn, J.W., Scripta Met., 14: p. 93 (1980).
47. Gershinskiy, A.Y., Fiz. metal. metalloved., 32(5): p. 1104 (1971).
48. Thuillard, M., Tran, L.T., and Nicolet, M.-A., Thin Solid Films, 166: p. 21 (1988).
49. CRC Handbook of Chemistry and Physics, ed. R.C. Weast. Vol. 66th Edition. 1985, CRC Press, Inc: Boca Raton, FL.
50. Tardy, J. and Tu, K.N., Phys. Rev. B, 32: p. 2070 (1985).
51. JCPDS Card No. 4-0836, Powder Diffraction File. 1996, International Center for Diffraction Data, Newtown Square, PA.